Proposed Inductor Power Loss Metric and Novel Embedded Toroidal Inductor for Integrated Voltage Regulators

Claudio Alvarez Barros, Prahalad Murali, Madhavan Swaminathan, *Fellow, IEEE*, Oishi Yusuke, Takashiro Junichi, Nagatsuka Ryo, and Naoki Watanabe

***Abstract*— High-density package-embedded inductors enable the miniaturization of high conversion ratio integrated voltage regulators (IVRs). In this work, we present a new embedded inductor structure along with a new performance metric called effective ac resistance per unit inductance and how the inductor sets constraints to the power stage topology. The proposed performance metric depends on the converter duty cycle and frequency and uses the inductor current harmonics, its inductance and resistance spectra, and the large-signal response to compute the inductor losses. No information of the inductor volume or its magnetic field distribution is used. The proposed embedded inductor structure shows a toroidal field distribution using a combination of slots through a magnetic sheet and vias through these slots. The new structure enables the fabrication of several inductors in the same magnetic substrate for multiphase IVR. The proposed inductors are fabricated and the metric is demonstrated with measurements using a high saturation magnetic material, where an interesting relation between the small- and large-signal losses was observed.**

***Index Terms*— 3-D inductors, buck converter, efficiency, embedded inductors, high-density integration, integrated voltage regulator (IVR), magnetic core inductors (MCIs), magnetic materials, package, power supply in package (PSiP), solenoid, toroid.**

I. Introduction

TRADITIONAL architectures for power delivery networks in servers and data centers, as shown in [1], require several downconversion stages to convert the grid voltage to usually 1-V dc required by processors (CPU). Fig. 1 shows a typical downconversion system that, when assuming an system on chip (SoC) power consumption of 90 W, shows a combined efficiency of 75%.

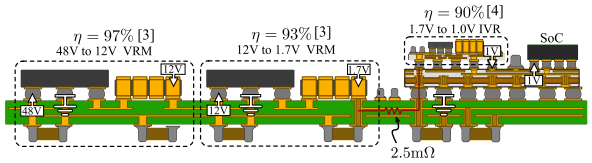

Fig. 1. Multistage 48–12–1.7 V with 1.7–1.0-V IVR downconversion.

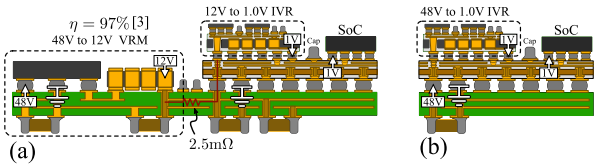

Fig. 2. Different power distribution networks. (a) Two-stage 48–12 V with 12–1.0-V IVR downconverter. (b) Single-stage 48–1.0-V IVR.

The losses can be reduced and the regulation bandwidth increased if a single-stage integrated voltage regulator (IVR) with input voltage greater than 5 V is integrated into the package, as shown in Fig. 2. In [5], an extensive analysis of the advantages that IVRs have for the next generation of microprocessors is presented. However, as the input voltage increases, the switching frequency must be reduced. As result, more inductance is required and the inductor design becomes challenging due to space constraints.

To reduce the losses and increase the switching frequency in a conventional hard switched buck converter, switched capacitors are combined with inductors to form a hybrid buck converter. In [6], several hybrid converters for 48–1 V are surveyed explaining their frequency, duty cycle, and efficiency limitation. What the hybrid topologies have in common is that they use switched capacitors along with the inductors to reduce the voltage stress and losses over the MOSFET and additionally extend the duty cycle. As shown in the survey, a switching frequency of 5 MHz can be achieved for 48–1 and 12–1 V.

Extensive research has been done for embedded inductors and IVRs, but mostly for low input voltage ($V_{IN} \leq 5$ V) with a typical conversion ratio of 1.7:1 V. With low input voltages, it is possible to use higher switching frequencies because low-voltage MOSFETs have lower parasitic capacitance and losses. With a conversion ratio of 1.7:1 V at frequencies

Manuscript received May 21, 2021; revised August 17, 2021; accepted September 11, 2021. Date of publication October 1, 2021; date of current version November 24, 2021. This work was supported in part by the Applications and Systems-Driven Center for Energy-Efficient Integrated NanoTechnologies (ASCENT), one of six centers in Joint University Microelectronics Program (JUMP), a Semiconductor Research Corporation (SRC) program sponsored by the Defense Advance Research Project Agency (DARPA); and in part by the Industry Consortium at the Packaging Research Center, Georgia Tech. Recommended for publication by Associate Editor V. Srinivas upon evaluation of reviewers' comments. *(Corresponding author: Claudio Alvarez Barros.)*

Claudio Alvarez Barros, Prahalad Murali, and Madhavan Swaminathan are with the 3D Systems Packaging Research Center, Georgia Institute of Technology, Atlanta, GA 30332 USA (e-mail: calvarez@gatech.edu).

Oishi Yusuke, Takashiro Junichi, and Nagatsuka Ryo are with Panasonic Corporation, Kadoma, Osaka 571-8686, Japan.

Naoki Watanabe is with Panasonic Industrial Devices Sales Company of America, Mountain View, CA 94043 USA.

Color versions of one or more figures in this article are available at https://doi.org/10.1109/TCPMT.2021.3116942.

Digital Object Identifier 10.1109/TCPMT.2021.3116942

2156-3950 © 2021 IEEE. Personal use is permitted, but republication/redistribution requires IEEE permission.
See https://www.ieee.org/publications/rights/index.html for more information.

Authorized licensed use limited to: Georgia Institute of Technology. Downloaded on December 09,2021 at 23:18:16 UTC from IEEE Xplore. Restrictions apply.

TABLE I
SUMMARY OF SE-BASED FORMULAS FOR POWER LOSS DENSITY (Wm^{-3}) CALCULATION [17]

Method	Square Exitation
SE	$k\, f^{\alpha} B_m^{\beta}$
MSE	$k\, f^{\alpha} B_m^{\beta} \frac{2^{\alpha-1} D^{\alpha-1} (1-D)^{1-\alpha}}{\pi^{2(\alpha-1)}}$
IGSE	$k_i\, f^{\alpha} B_m^{\beta} 2^{\beta} [D^{1-\alpha} + (1-D)^{1-\alpha}]$
WcSE	$\frac{\pi}{4} k\, f^{\alpha} B_m^{\beta}$

above 10 MHz, the required inductance can be lower than 35 nH. Air core inductors, as shown in [3], have been used at very high frequencies above 100 MHz with the advantage of the elimination of the magnetic losses. Thin-film inductors, as shown in [7]–[13], have been used for frequencies above 10 MHz with inductance in the range of 10–50 nH and dc resistance in the range of 20–300 mΩ. For an input voltage of 12 V or above, the switching losses prevent the converter to operate above a few megahertz, with a typical frequency range of 250 kHz–2 MHz. At 2 MHz and a current ripple of 0.5 A, the required inductance would be 450 nH. For point-of-load regulators that operate at 2 MHz or below, printed circuit board (PCB) embedded inductors have been proposed in [14] and [15] with inductance over 600 nH and inductance density between 3 and 7 nH/mm^2. In the review paper [16], several other types of inductors and magnetic materials are surveyed and compared using dc and ac performance metrics, exposing their advantages and weaknesses.

Typically, the amount of inductance is driven by a maximum inductor current ripple and frequency. However, for high-performance voltage regulators, the design must be based on the inductor efficiency with the maximum current ripple, maximum frequency, and minimum duty cycle as a constraint. In [17], a comparison of inductor cores loss calculation methods is presented, including the Steinmetz equation (SE), modified SE (MSE), the improved generalized SE (IGSE), and the waveform coefficient SE (WcSE). These analyses are conducted for nonsinusoidal excitations in switched-mode power supplies at a frequency of 10 kHz. Only the methods MSE and IGSE can predict the core loss increment when the switching duty cycle moves away from 50%. This increase of losses is the result of the inductor current harmonics. However, as shown in [17] through measurements, the MSE and IGSE methods can show an error of $+10\%$ at 0.5 duty cycle and -25% at 0.1 duty cycle. In Table I, it has shown the summary of formulas for the most common methods.

In [23], an improved SE (ISE) method is presented where the square excitation is separated into two pulses with their frequencies related to the duty cycle. As shown with measurements, this method shows excellent accuracy at 100 kHz, and its accuracy is only slightly reduced at a frequency of 25 kHz. This model has the next formula

$$P_c = \frac{\pi}{4} k_1\ D \left(\frac{f}{\text{2-D}}\right)^{\alpha_1} B_m^{\beta_1} + \frac{\pi}{4} k_2 (1-D) \left(\frac{f}{2(1-D)}\right)^{\alpha_2} B_m^{\beta_2}.$$

In [23], it is also discussed the drawbacks of the different methods, where they are mainly reviewed by its accuracy over waveform, duty cycle, and frequency.

Even though the ISE method presented in [23] can have very good results, it shares the same complications as the other methods when they need to be applied to embedded inductors. We see two difficulties to apply these methods: 1) embedded inductors usually have no defined volume, which is a problem since these methods give a power loss density Wm^{-3}, and 2) the magnetic field in the magnetic substrate is not uniform making difficult to choose the value of B_m.

This article is an extension of the work published in [18], where a novel embedded toroidal inductor and a new inductor metric called effective ac resistance per unit inductance or R_{acx} were proposed. The objectives, of this power loss calculation method, are: 1) relate the inductor core losses to circuit quantities such as inductance L and inductor current ripple Δi_L, instead of magnetic quantities such as the magnetic flux $\vec{B}$; 2) include the effect of the duty cycle allowing the codesign with the power stage topology; 3) characterize the small- and large-signal losses in the megahertz regime; and 4) remove the dependency on the inductor volume. With the proposed method, no acknowledgment on the inductor volume and magnetic field is required, making its application easier. In addition, in this work, we present several embedded inductor structures that are analyzed with the proposed metric.

This work presents an in-depth analysis, including detailed derivation of the small-signal effective ac resistance per unit inductance r_{acx} metric, inductor requirements for a target inductor efficiency using the R_{acx} framework, detailed analysis of the inductor structure model, small-signal measurements and simulation for seven different inductors designs, saturation current and large-signal measurements of the inductors, and comparison of the small- and large-signal losses.

This article is structured as follows. Section II describes the new inductor metric. Section III provides a design framework, based on the R_{acx} metric, to obtain the inductor properties for a given input to output voltage, frequency, duty cycle, and inductor efficiency. Section IV describes the novel embedded toroidal inductors. Section V shows the fabrication and measurement setups. Sections VI–VIII show the small-signal measurement results with and without dc bias current and the large-signal response. Finally, Section IX concludes and discusses the results.

II. PROPOSED INDUCTOR METRIC

The basic form of a buck converter's topology is shown in Fig. 3, along with the two circuit states and the inductor current ripple waveform. There are two states: between $0 < t < DT_s$ when the high-side switch is closed and the low-side switch is open and between $DT_s < t < T_s$ when the high-side switch is open and the low-side switch is closed. Here, $0 < D < 1$ is the duty cycle and T_s is the switching period.

The inductor introduces losses in the exchange of energy between the source V_g and the load R_{LD}. We can decompose the inductor power loss into three parts, as shown in (1): 1) dc conduction losses $P_{L,\mathrm{dc}}$; 2) eddy current losses (in both copper and magnetic material) $P_{L,\mathrm{ac}}$; and 3) magnetic core losses $P_{L,H}$ (due to hysteresis)

$$P_L = P_{L,\mathrm{dc}} + P_{L,\mathrm{ac}} + P_{L,H}. \tag{1}$$

Authorized licensed use limited to: Georgia Institute of Technology. Downloaded on December 09,2021 at 23:18:16 UTC from IEEE Xplore. Restrictions apply.

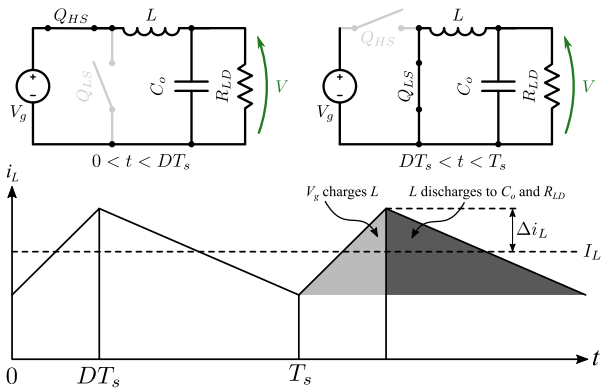

Fig. 3. Simple buck converter topology and its operation.

The hysteresis loss $P_{L,H}$ is given by the B–H hysteresis loop where the density of energy lost per switching cycle is $U = \int \vec{H} \cdot d\vec{B}$ [Jm^{-3}]. The power loss is found by multiplying U by the effective inductor volume and switching frequency. However, as shown in [17] and [19], the hysteresis losses are also affected by the duty cycle D. Several methods, including the MSE, generalized SE (GSE), ISE, IGSE, and wave-coefficient SE, have been used to model the inductor core losses when a nonsinusoidal excitation is applied. These models require knowing the magnetic flux $\vec{B}$, and however, the value of $\vec{B}$ can be nonuniform inside the inductor and therefore difficult to quantify. In addition, the effective magnetic volume is required, which for embedded inductors may not be defined. In this work, we study the relation of more circuit-friendly quantities, such as inductance L and inductor current ripple Δi_L, to model the inductor losses with nonsinusoidal currents. The inductance L already lumped the effective inductor volume and energy-storing capacity in its volume, and the current ripple Δi_L is related to the span of magnetic field. Both L and Δi_L are easier to measure.

We start by deriving an expression to quantify the small-signal losses $P_{L,\mathrm{dc}}$ and $P_{L,\mathrm{ac}}$ and to then compare it with the large-signal losses P_L. To compute $P_{L|s} = P_{L,\mathrm{dc}} + P_{L,\mathrm{ac}}$, we start by considering the inductor current Fourier sine expansion given by

$$i_L(t) = I_L + \sum_{n=1}^{N} \frac{2\Delta i_L}{D(1-D)} \frac{\sin(n\pi D)}{(n\pi)^2} \sin\left(2n\pi \frac{t}{T_s}\right) \quad (2)$$

where Δi_L is the inductor current ripple, I_L is the inductor dc current, and D and T_s are the switching duty cycle and period, respectively. The current ripple is given by the next expression

$$\Delta i_L = \frac{V}{2L}(1-D)T_s. \quad (3)$$

The average dc and small-signal power loss in the inductor due to an equivalent resistance R_L is

$$P_{L|s} = \frac{1}{T_s}\int_0^{T_s} i_L(t) v_{\mathrm{RL}}(t) dt$$

where $i_L(t)$ is the instantaneous inductor current and $v_{\mathrm{RL}}(t)$ is the instantaneous voltage drop over the inductor's equivalent resistance R_{ac} . However, the inductor resistance is a function of frequency. Therefore, we will have a dc power loss, due to the copper dc resistance, and an ac power loss, due to the magnetic and copper losses at every frequency harmonics.

The dc power loss is

$$P_{L,\mathrm{dc}} = I_L^2 R_{\mathrm{dc}}. \quad (4)$$

To calculate the small-signal ac power loss, first, we need to consider the next expression for $v_{\mathrm{RL}}(t) = i_L(t) R_{\mathrm{ac}}$

$$v_{\mathrm{RL}}(t) = \sum_{m=1}^{M} \frac{2\Delta i_L}{D(1-D)} \frac{\sin(m\pi D)}{(m\pi)^2} \sin\left(2m\pi \frac{t}{T_s}\right) R_{\mathrm{ac}}\left(\frac{m}{T_s}\right) \quad (5)$$

and then, $P_{L,\mathrm{ac}}$ is

$$P_{L,\mathrm{ac}} = \frac{2\Delta i_L^2}{D^2(1-D)^2} \sum_{n=1}^{N} \frac{\sin^2(n\pi D)}{(n\pi)^4} R_{\mathrm{ac}}\left(\frac{n}{T_s}\right). \quad (6)$$

The variable $r_{\mathrm{acx}}(D, f)$ is defined here as the small-signal effective ac resistance per unit inductance with units of $\Omega\,\mathrm{H}^{-1} = s^{-1}$ and is given as follows:

$$r_{\mathrm{acx}} = \frac{2}{D^2(1-D)^2} \sum_{m=1}^{M} \frac{\sin^2(m\pi D)}{(m\pi)^4} \frac{R_{\mathrm{ac}}\,(mf_s)}{L(f_s)} \quad (7)$$

and corresponds to a loss ratio normalized to the inductance and current ripple squared at the switching frequency f_s. This normalization makes it independent of the volume used by the inductor, but it is also independent of the current ripple.

We can now combine (1), (4), (6), and (7) to obtain the next inductor power loss expression

$$P_L = I_L^2 R_{\mathrm{dc}} + \Delta i_L^2\, L(f_s)\, r_{\mathrm{acx}}(D, f_s) + P_{L,H}. \quad (8)$$

Since $\Delta i_L^2\, L(f_s)$ has units of joule and r_{acx} corresponds to an energy loss factor and is a measure proportional to how much energy is lost per cycle.

Using the inductor presented in the following, it was observed from the measurements that $P_{L,\mathrm{ac}}$ and $P_{L,H}$ can be related by a factor $\kappa(f_s)$ such that $P_{L,H} = (\kappa - 1)P_{L,\mathrm{ac}}$, giving as results

$$P_L = I_L^2 R_{\mathrm{dc}} + \Delta i_L^2\, L(f_s)\, \kappa(f_s) r_{\mathrm{acx}}(D, f_s) \quad (9)$$

$$P_L = I_L^2 R_{\mathrm{dc}} + \Delta i_L^2\, L(f_s)\, R_{\mathrm{acx}}(D, f_s) \quad (10)$$

and it will be shown that r_{acx} and R_{acx} (corresponding to the small- and large-signal loss ratio, respectively) are indeed independent of the amount of inductance and current ripple. The factor κ is the large-to-small-signal loss ratio and is defined as follows:

$$\kappa = \frac{R_{\mathrm{acx}}}{r_{\mathrm{acx}}} \quad (11)$$

with the values of r_{acx} obtained from the small-signal inductance and resistance spectra, and the values of R_{acx} obtained from the large-signal excitation of the inductor using a buck converter. Since this is a hybrid approach, where r_{acx} is derived and κ is completely determined by empirical methods, more experimentation needs to be done to understand how κ changes with respect to f_s, Δi_L, and D for other magnetic materials.

Authorized licensed use limited to: Georgia Institute of Technology. Downloaded on December 09,2021 at 23:18:16 UTC from IEEE Xplore. Restrictions apply.

In Section III, we show how to use this metric as a design tool to find the required inductor properties for a target inductor efficiency.

III. Requirements of Inductance and R_{acx}

Every switching cycle the inductor is charged with additional energy ΔE_L, which is then transferred to the load. This amount of energy is given by (12), provided that the inductor is not saturated and the inductance remains constant over the integration limits

$$\Delta E_L = \int_{i_L(0)}^{i_L(DT_s)} L\, i_L di_L = 2LI_L \Delta i_L = I_L V(1-D)T_s. \quad (12)$$

The inductor power loss expression can be rewritten using the delta energy expression (12) as follows:

$$P_L = I_L V\alpha + 2L(f_s) I_L \Delta i_L f_s \beta \quad (13)$$

where α is the dc loss factor due to the parasitic dc resistance and β is the inductor ac loss factor and tells how much of the energy stored in the inductor is lost when it is released to the load. Both factors are unitless. The variables α and β are defined as

$$\alpha = \frac{I_L}{V} R_{\text{dc}} \quad (14)$$

$$\beta = \frac{\Delta i_L}{2I_L f_s} R_{\text{acx}}. \quad (15)$$

From (10) (and as will be shown in Section VIII) with 0 A of dc current, R_{acx} can be given by $R_{\text{acx}} = P_L/\Delta i_L^2\ L$, and therefore, it is not limited to the small-signal losses, but the total inductor ac losses. From (12), we note that $2LI_L\Delta i_L f_s = I_L V(1-D)$, and then, we can simplify the power loss formula (13) as follows:

$$P_L = I_L V(\alpha + (1-D)\beta). \quad (16)$$

The inductor efficiency η_L is defined as the ratio of the power delivered to the load over the power delivered to the inductor

$$\eta_L = \frac{I_L V}{I_L V + P_L} = \frac{1}{1+\alpha+(1-D)\beta}. \quad (17)$$

The power-related equivalent series resistance R_L of the inductor is defined by

$$R_L = \frac{P_L}{I_{L,\text{RMS}}^2} = \frac{I_L V}{I_{L,\text{RMS}}^2}(\alpha + (1-D)\beta). \quad (18)$$

Let us denote I_M as the output dc current at maximum inductor efficiency, and then, the inductor power loss at maximum efficiency is given by

$$P_L = I_M V\left(\frac{1}{\eta_L} - 1\right). \quad (19)$$

From the inductor efficiency expression (17), to maximize the efficiency with respect to the load current I_M, we need to minimize the expression $\alpha + (1-D)\beta$. From the definition of α and β, we have

$$\begin{aligned}\frac{d}{dI_M}\left\{\frac{I_M R_{\text{dc}}}{V} + (1-D)\frac{\Delta i_L}{2I_M f_s} R_{\text{acx}}\right\} &= 0\\ = \frac{R_{\text{dc}}}{V} - (1-D)\frac{\Delta i_L}{2I_M^2, f_s} R_{\text{acx}} &= 0\\ = \alpha - (1-D)\beta &= 0\end{aligned}$$

and this result means that, to obtain the maximum efficiency for a given output dc current I_M, the dc and ac losses must be equal, hence $\alpha = (1-D)\beta$.

Expression (8) is rewritten by replacing the current ripple using (3)

$$P_L = I_M^2 R_{\text{dc}} + \frac{V^2}{4Lf_s^2}(1-D)^2 R_{\text{acx}} \quad (20)$$

then R_{dc} is obtained by

$$R_{\text{dc}} = \frac{P_L}{2}\frac{1}{I_M^2} \quad (21)$$

and this sets the upper bound for the dc resistance. Naturally, any lower value will yield lower losses. For the ac loss $P_{L,\text{ac}}$, we obtain the next condition

$$\frac{V^2(1-D)^2}{4Lf_s^2} R_{\text{acx}} = \frac{P_L}{2}. \quad (22)$$

The two inductor parameters from (22) are L and R_{acx}. The values of duty cycle D and switching frequency f_s are set by the application conversion ratio and are decided as design choices. Therefore, the previous expression can be written as

$$\frac{\widetilde{R}_{\text{acx}}}{L} = \frac{P_L}{2}\frac{4f_s^2}{V^2(1-D)^2}\left[\frac{\Omega}{\text{H}^2}\right] \quad (23)$$

where $\widetilde{R}_{\text{acx}}$ is the maximum required value, not the measured one. Higher values of $\widetilde{R}_{\text{acx}}$ allow for less efficient magnetic materials since the measured R_{acx} needs to be lower than $\widetilde{R}_{\text{acx}}$. Since $\widetilde{R}_{\text{acx}}$ and its relation to L has an inverse quadratic dependence on $1-D$, an accurate value for the duty cycle is required.

As an application example, we consider a series capacitor (SC) buck converter [20], and the GaN model presented in [21] along with SPICE simulation, to calculate the duty cycle. For 48–1-V conversion, we consider a four-phase SC buck converter providing a four-times duty cycle extension to obtain $D = 0.0925$. For 12–1-V conversion, we consider a two-phase SC buck converter providing two times duty cycle extension to obtain $D = 0.1834$. Table II shows the conversion parameters used in this analysis.

With accurate values of the duty cycle D, we can obtain the $\widetilde{R}_{\text{acx}}$ to inductance L ratio. Figs. 4 and 5 show the values of $\widetilde{R}_{\text{acx}}$ and Δi_L versus inductance required for conversion ratios of 48–1 and 12–1 V at different frequencies.

From these figures, we can extract the required inductor properties, which are summarized in Table III.

In comparison, Fig. 6 shows the required $\widetilde{R}_{\text{acx}}$ and inductance for 1.7–1-V conversion ratio. At 5 MHz, this conversion ratio only requires 70 nH with $\widetilde{R}_{\text{acx}} = 2.8$ mΩ/nH. For a high

Authorized licensed use limited to: Georgia Institute of Technology. Downloaded on December 09,2021 at 23:18:16 UTC from IEEE Xplore. Restrictions apply.

TABLE II

PARAMETERS TO COMPUTE THE REQUIRED R_{acx} AND INDUCTANCE L FOR TWO HIGH CONVERSION RATIOS

Parameter	For 48 V to 1V	For 12 V to 1V
Target η_L	95%	
Target f_s	5 MHz	
Target V	1 V	
I_M per-phase	1.875 A	
P_L	98.7 mW	
R_{DC}	14 mΩ	
D	9.25 %	18.34 %

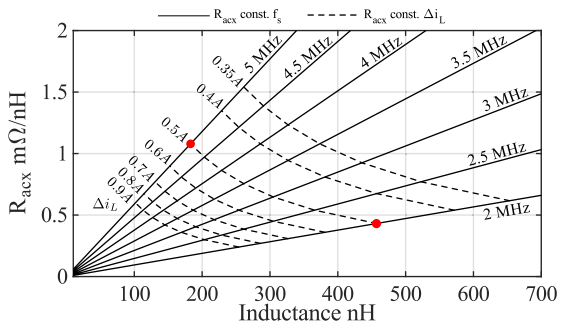

Fig. 4. $\widetilde{R}_{\text{acx}}$ versus L for $V_g = 48$ V, $D = 0.0925$, and $R_{\text{dc}} = 14$ mΩ.

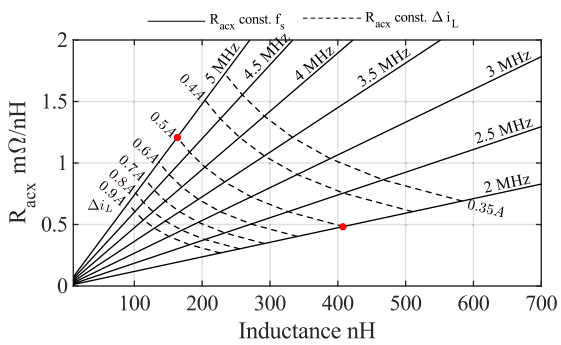

Fig. 5. $\widetilde{R}_{\text{acx}}$ versus inductance for $V_g = 12$ V, $D = 0.1834$, and $R_{\text{dc}} = 14$ mΩ.

TABLE III

INDUCTOR REQUIREMENTS WITH $\Delta i_L = 0.5$ A AND $R_{\text{DC}} = 14$ mΩ

V_g	D	f_s MHz	L nH	$\widetilde{R}_{acx}$ mΩ/nH
48	0.0925	5.0	183	1.079
48	0.0925	2.0	457	0.432
12	0.1834	5.0	163	1.208
12	0.1834	2.0	408	0.482

conversion ratio converter, more than twice the inductance with less than half $\widetilde{R}_{\text{acx}}$ is required.

Given the very low required dc resistance, in Section IV, we present the minimal implementation of an embedded toroidal inductor with just two turns. This inductor structure is further expanded to increase its inductance while at the same time keeping its dc resistance at its minimum. r_{acx} for the same magnetic material is compared for inductors with different amounts of inductance and different structures.

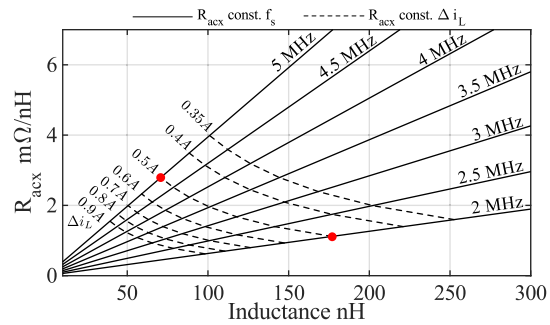

Fig. 6. $\widetilde{R}_{\text{acx}}$ for $V_g = 1.7$ V, $D = 0.646$, and $R_{\text{dc}} = 14$ mΩ.

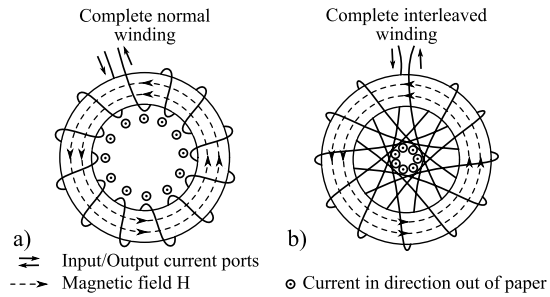

Fig. 7. Types of toroidal inductor winding. (a) Complete normal winding. (b) Complete interleaved winding.

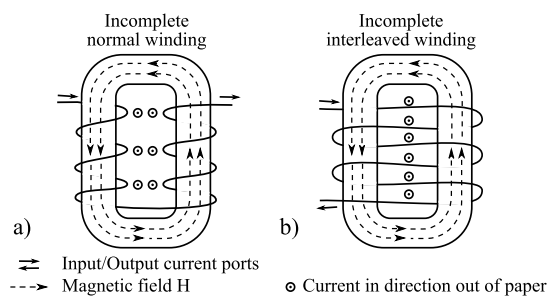

Fig. 8. Types of toroidal inductors with incomplete winding. (a) Incomplete normal winding. (b) Incomplete interleaved winding.

IV. EMBEDDED TOROIDAL INDUCTOR DESIGN

As shown in [22], for an inductor to be effectively embedded in a package, it needs to have a closed magnetic path, which means that all the magnetic fields must go through the magnetic material and not air. An example of a closed magnetic path inductor is a toroidal inductor, as shown in Fig. 7(a) and (b). Toroidal inductors with many vias and windings are difficult to fabricate, limiting the smallest critical dimensions of the inductor. They can be simplified considerably if the windings are arranged longitudinally, as shown in Fig. 8. They can be thought of as a single incomplete toroidal inductor or two solenoid inductors. They are called incomplete because the winding only covers part of the core.

When the inductor is built using a magnetic sheet as the substrate, both solenoids and toroids show a closed magnetic path. This allows the fabrication of one or more of the inductors as shown in Fig. 8 on the same magnetic substrate eliminating the need to cut discrete magnetic cores. In this work, several configurations derived from the concept shown in Fig. 8 were fabricated. Fig. 9 shows four interleaved

Authorized licensed use limited to: Georgia Institute of Technology. Downloaded on December 09,2021 at 23:18:16 UTC from IEEE Xplore. Restrictions apply.

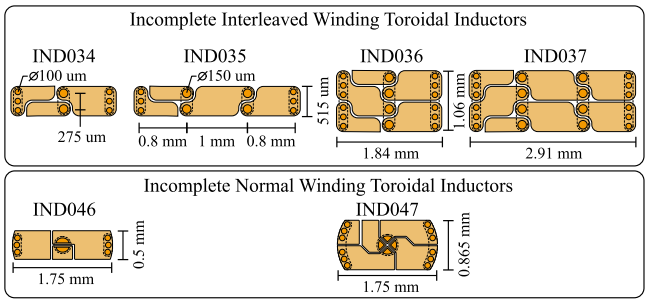

Fig. 9. Normal and interleaved toroidal inductor configurations.

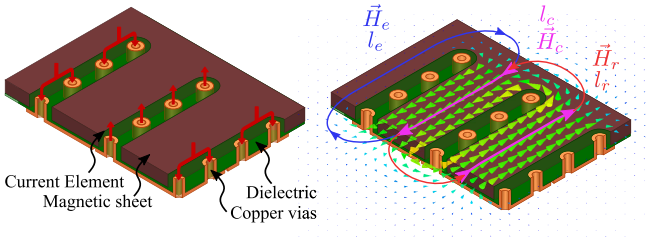

Fig. 10. Details of inductor current elements distributed in vias.

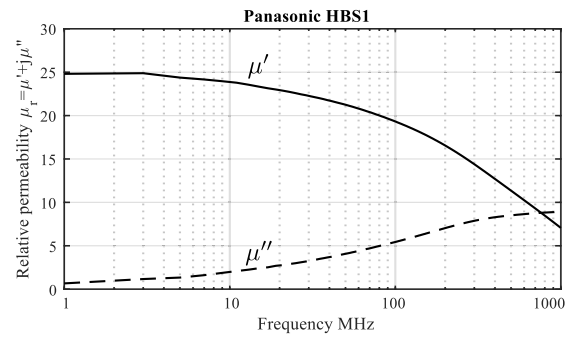

Fig. 11. Permeability spectra of Panasonic HBS1.

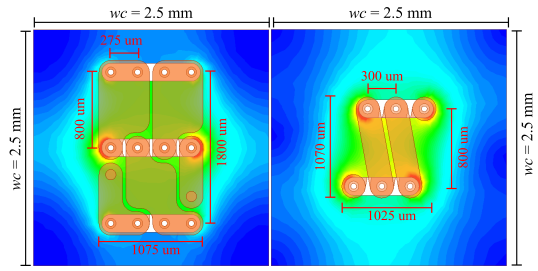

Fig. 12. Comparison of solenoid and toroid using HBS1 magnetic sheets.

windings (IND034, IND035, IND036, and IND037) and two normal winding (IND046 and IND047) toroidal inductors.

The interleaved windings allow chaining multiple structures providing more degrees of freedom to customize the amount of required inductance. However, the incomplete normal winding inductor shows a higher inductance density due to the shorter magnetic path length (in the central vias) when compared to the interleaved version. As will be shown later, IND047 compared to IND036 has more inductance with a similar dc resistance.

Let us consider the inductor IND036, which is shown in more detail in Fig. 10. Several vias are arranged in slots drilled through a magnetic sheet substrate to couple their magnetic field and provide electrical isolation. It has N current elements in the center and $N/2$ current elements on each side. The magnetic field H is built around the central vias with an elongated toroidal field distribution, and the magnetic field is confined to the inductor structure even if the magnetic sheet is much larger. Considering a large enough magnetic substrate, we can find a path $\vec{l}$ such that it is tangent to the magnetic field $\vec{H}$, and then, Ampere's law $\oint \vec{H} \cdot \vec{dl} = Ni$ can be simplified to $\oint H\, dl = Ni$, where N is the number of enclosed vias, i is the current through a via, and H is constant along the integration path l_c. We can write the next expressions

$$2H_c l_c + 2\int_{l_r} H_r dl = 4i \quad \text{and} \quad H_c l_c + \int_{l_e} H_e dl = 2i$$

and solving for $\int_{l_e} H_e dl$, we obtain

$$\int_{l_e} H_e dl = \int_{l_r} H_r dl \tag{24}$$

and given that the path length $l_e > l_r$, then the average values of $\overline{H}_e < \overline{H}_r$ outside of the inductor. Far from the inductor, H_e becomes very small. To see this, let us write the limit form of (24) as follows:

$$\lim_{\Delta l_{e|n} \to 0} \sum_{n=0}^{N} H_{e|n} \Delta l_{e|n} = \lim_{\Delta l_{r|m} \to 0} \sum_{m=0}^{M} H_{r|m} \Delta l_{r|m}. \tag{25}$$

If we consider $\Delta l_{e|n} = l_e/N$ for every n and $\Delta l_{r|m} = l_r/M$ for every m, then we have

$$\lim_{N \to \infty} \sum_{n=0}^{N} H_{e|n} \frac{l_e}{N} = \lim_{M \to \infty} \sum_{m=0}^{M} H_{r|m} \frac{l_r}{M} \tag{26}$$

and finally,

$$\frac{\lim\limits_{N \to \infty} \dfrac{\sum_{n=0}^{N} H_{e|n}}{N}}{\lim\limits_{M \to \infty} \dfrac{\sum_{m=0}^{M} H_{r|m}}{M}} = \frac{\overline{H}_e}{\overline{H}_r} = \frac{l_r}{l_e}. \tag{27}$$

To demonstrate and verify the inductors and the metric presented in this work, a high-saturation metal-composite magnetic material (courtesy of Panasonic) in the form of a magnetic sheet with a thickness of 400 μm is used. Fig. 11 shows the measured permeability of the material HBS1, obtained using a 1-MHz-to-3-GHz impedance analyzer Keysight E4991A. The inductor IND036 is first simulated and compared to a solenoid inductor, and then, in Section V, the fabrication results for all the inductors are presented.

Fig. 12 shows the top view of the magnetic field H of a solenoid (right) and the toroidal inductor of this work (left) in a magnetic sheet size of 2.5 × 2.5 × 0.4 mm, both with the same amount of inductance. Here, we can see the complications to determine inductor volume and the magnetic field B_m over this volume. The magnetic field is not uniform and the volume is not well defined. This makes difficult to use the different methods based on the SE.

Authorized licensed use limited to: Georgia Institute of Technology. Downloaded on December 09,2021 at 23:18:16 UTC from IEEE Xplore. Restrictions apply.

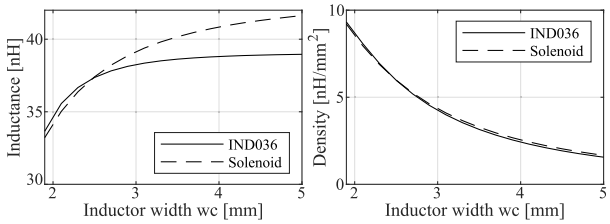

Fig. 13. Inductance (left) and Inductance density (right) at 10 MHz of the simulated solenoid and IND036 as a function of the substrate width.

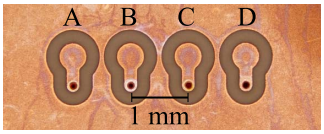

Fig. 14. Test structure for direct via drilling evaluation.

The dc resistance for the solenoid is 23 mΩ, and for the toroid, it is 24.7 mΩ. Fig. 13 shows the inductance as a function of the substrate width wc. Even though the solenoid seems smaller, its size must be defined according to the space required to build up its inductance, not just its geometrical bounding box. From Fig. 13, it is observed that the solenoid inductor requires the same space as the IND036, and however, the inductor IND036 has more control over the space it will use.

The coupling between inductors in a magnetic sheet can be controlled by the use of slots cut in the magnetic substrate. When the vias of two inductors share the same slot, their coupling is maximized. When the two inductors do not share the same slot, their coupling is minimized. In this way, the coupling between inductors can be controlled. When the coupling is not required, the slots can be omitted and the vias can be drilled directly on the magnetic substrate. However, there are two requirements to avoid the use of slots: the material must be compatible with electroless copper deposition (as it is part of the fabrication process as described in [18]), and the magnetic material must be nonconductive. Fig. 14 shows a test structure with vias directly drilled in the magnetic material. With the material HBS1, it was measured an open-circuit across any of the vias. Therefore, with this material, the slots could be omitted, provided that the metallic filler size is smaller than the via separation. A different high-permeability ($\mu_r = 180$) metal composite magnetic material, though not used in this work, showed a resistance of 5.5 Ω between vias B and C and 8 Ω between vias A and D. Coupled inductors are not discussed in this work.

With this inductor design, several inductors can be fabricated in the same magnetic substrate for multiphase package IVR modules, increasing the level of power delivery granularity. The integration between the embedded inductors and the power stage circuitry, to form the package IVR, is shown in the cross section in Fig. 15.

In Sections V–VIII, it is shown the fabrication and measurement of these embedded inductors. We have compared the results of r_{acx} using the small-signal inductance and resistance spectra, with the measurement of R_{acx} using the large-signal response in a buck converter. We use a high saturation magnetic material to make sure that the current ripple only traces a minor loop in the B–H curve and the inductor does not saturate.

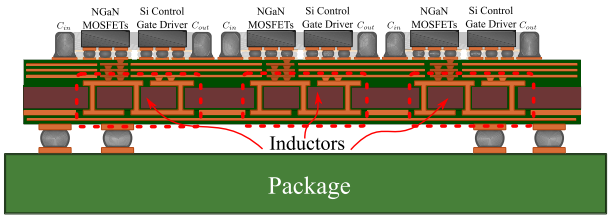

Fig. 15. Multiphase IVR integration.

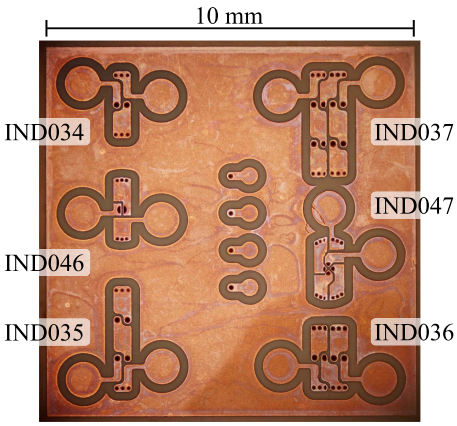

Fig. 16. Fabrication result before the solder mask is applied.

TABLE IV
INDUCTORS DC RESISTANCE IN mΩ WITH 25-μm ELECTROPLATED COPPER THICKNESS

IND034	IND046	IND035	IND036	IND047	IND037
14.3	13.6	21.3	24.9	29.0	39.3

V. FABRICATED INDUCTORS AND MEASUREMENT SETUP

The six inductor designs shown in Fig. 9 were fabricated using the HBS1 material with a thickness of 400 μm. In this substrate, slots are first drilled to make sure that no magnetic material is between the vias, so they are not electrically connected. The slots are then filled with ABF GX92 dielectric and the vias are drilled in the slots to form the inductor. This results in a via-in-slot through magnetic substrate embedded inductor. The complete fabrication process was previously presented in [18]. The top view of the fabricated inductors is shown in Fig. 16. Table IV shows the measured dc resistance. The simulated dc resistance was fit to the measurements to estimate an electroplated copper conductance of 4.2 S/m. A solder mask layer was applied to protect the inductor and expose only the circular pad.

A test board for measurements was designed and fabricated. The board allows to measure the small signal with and without dc bias current using a vector network analyzer (VNA) and the large-signal response using a buck converter (with GaN MOSFET) that allows an independent control of input voltage, frequency, and duty cycle. Fig. 17 shows the measurement

Authorized licensed use limited to: Georgia Institute of Technology. Downloaded on December 09,2021 at 23:18:16 UTC from IEEE Xplore. Restrictions apply.

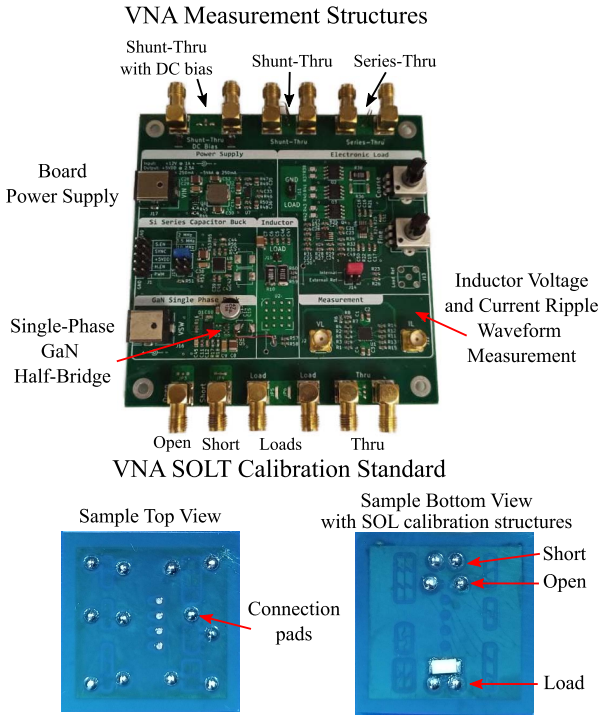

Fig. 17. Measurement board.

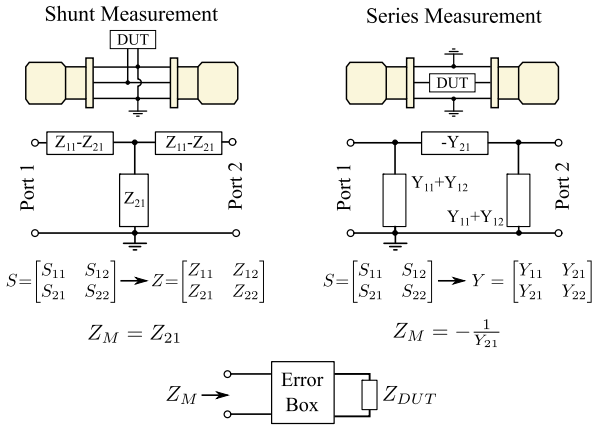

Fig. 18. Inductance model for shunt-thru and series-thru measurement.

board. To measure the dc resistance, a four-wire method and multimeter from Hewlett Packard model 34401A were used. To measure in the range of 10 MHz–1 GHz, a VNA from Agilent Technologies model E8363B was used, and in the range of 100 kHz–100 MHz, an open-source low-frequency VNA, called nanoVNA V1, was used.

To cover a broad frequency range from 100 kHz to 1 GHz, two measurement setups as shown in Fig. 18 are needed. Below 100 MHz, a shunt-thru method is used because the inductor impedance below 10 MHz is lower than 50 Ω. Above 10 MHz, a series-thru method is used as the inductor impedance above 100 MHz is greater than 50 Ω. As a sanity check, both methods must give the same result between 10 and 100 MHz. In addition, a two-level calibration is needed. A short, open, load, and thru (SOLT) calibration is performed at the end of the VNA SMA connection ports 1 and 2, and

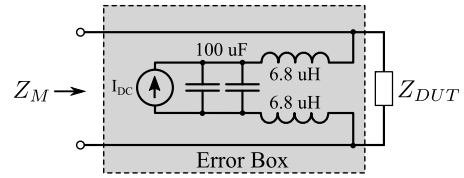

Fig. 19. Small-signal dc bias setup.

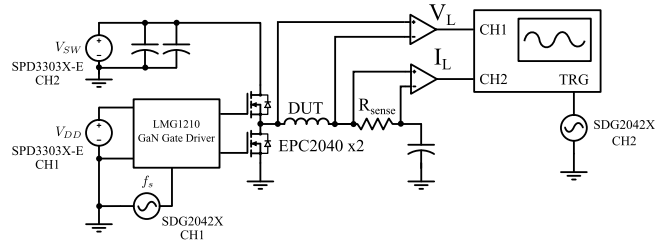

Fig. 20. Large-signal measurement setup.

a short, open, and load (SOL) calibration structure fabricated in the same inductor sample, as shown in Fig. 17, is used to find the error box shown in Fig. 18.

Fig. 19 shows the dc bias measurement setup, where an isolated current source from Siglent model SPD3303X-E applies a bias current to the inductor, and two filter inductors (Murata MPXV1D0624L6R8) of 6.8 μH with a self-resonance frequency of 18 MHz and saturation current of 4.5 A are used to provide a much larger impedance seen toward the current source in comparison to the inductor to be measured. An SOL calibration is used to find the error box and remove the effect of the bias setup in the inductor measurement. Only a shunt-thru measurement is performed in the range of 100 kHz–100 MHz.

The large-signal measurement setup is shown in Fig. 20. For the large-signal measurements, a dual isolated power supply from Siglent model SPD3303X-E was used to power the board and the MOSFETs. A signal generator from Siglent model SDG2042X was used to generate the MOSFET switching signal and oscilloscope trigger. An oscilloscope from Siglent model SDS1202X-E with 1 Gs/s was used to record the inductor voltage and current waveform. The oscilloscope is externally triggered to make sure that both waveforms are captured at the same time event reducing any phase shift between them. In addition, the waveforms are captured in averaged mode.

The inductor current and voltage waveforms are obtained by a pair of 300-MHz bandwidth differential amplifiers OPA2673, which were calibrated to obtain its gain and dc offset. The multiplication of these two waveforms gives the instantaneous inductor power. The inductance is calculated as

$$L = \frac{V_L \Delta_t}{\Delta i_L} \tag{28}$$

where V_L is the average inductor voltage during the selected interval Δ_t. The inductor power loss is obtained with the average of the inductor power waveform

$$P_L = \frac{1}{t_1 - t_0} \int_{t_0}^{t_1} v_L(t) i_L(t) dt. \tag{29}$$

Authorized licensed use limited to: Georgia Institute of Technology. Downloaded on December 09,2021 at 23:18:16 UTC from IEEE Xplore. Restrictions apply.

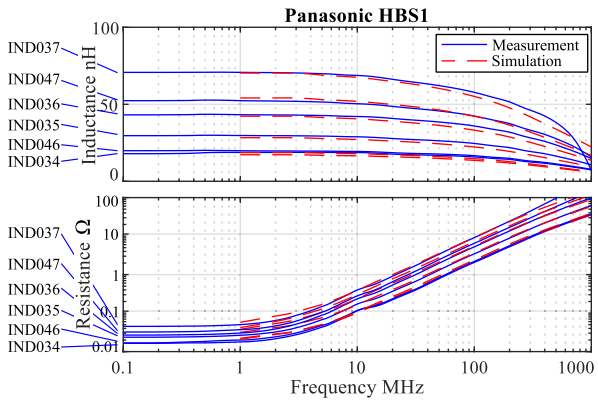

Fig. 21. Simulation and measurement results.

TABLE V
MEASURED INDUCTOR PARAMETERS AT $f_s = 3$ MHz

Inductor	L [nH]	R_{AC} [mΩ]	R_{DC} [mΩ]
IND034	18.8	27.4	14.3
IND046	19.6	30.5	13.6
IND035	29.6	41.5	21.3
IND036	43.0	51.6	24.9
IND047	51.9	61.9	29.0
IND037	70.3	86.8	39.3

Fig. 22. Discrete toroidal inductor for r_{acx} comparison.

With the large-signal inductance, power loss, and current ripple, it is possible to obtain the R_{acx} value.

VI. Small-Signal Measurements

The inductors were simulated with ANSYS Maxwell using the measured material properties shown in Fig. 11 and then compared to the measurements. The simulated (in red) and measured (in blue) inductance and resistance are shown in Fig. 21. Table V shows the inductance and resistance values at 3 MHz.

To study how the r_{acx} metric behaves when the inductor geometry is changed, a complete discrete toroidal inductor was fabricated and measured, as shown in Fig. 22. Fig. 23 shows r_{acx} computed from the inductance and resistance spectra. The r_{acx} curves for all the embedded inductors (there are six black lines at each frequency, one for each embedded inductor) are very close to each other. This shows that this metric is not very sensitive to geometric changes and inductance values.

We note that the toroid of Fig. 22 has a lower r_{acx} at lower frequencies. To understand this, in the expression (7), the term R_{ac}/L needs to be separated between the air core contribution of the inductance L_{air} and resistance R_{air} and the increment, due to the inclusion of the magnetic material, of the inductance

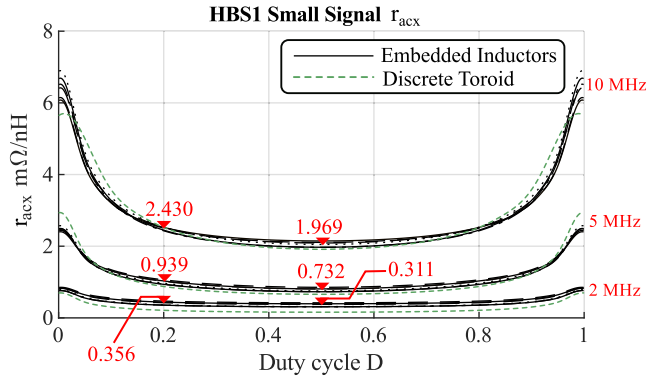

Fig. 23. r_{acx} for material HBS1.

ΔL_{mag} and resistance ΔR_{mag}. Let us use the subscript 1 in $L_{air,1}$, $\Delta L_{mag,1}$, and $\Delta R_{mag,1}$ to denote the values per turns N, and then, we have

$$\frac{R_{ac}}{L} = \frac{R_{air} + \Delta R_{mag}}{L_{air} + \Delta L_{mag}} = \frac{N\, R_{air,1} + N^2 \Delta R_{mag,1}}{N^2\, L_{air,1} + N^2\, \Delta L_{mag,1}}. \quad (30)$$

R_{air} is only proportional to the number of turns, as it is due to the copper resistance and the skin depth. The previous expression can be simplified to

$$\frac{R_{ac}}{L} = \frac{\frac{R_{air,1}}{N} + \Delta R_{mag,1}}{L_{air,1} + \Delta L_{mag,1}} \quad (31)$$

and therefore, with a larger number of turns or magnetic losses, the ratio R_{ac}/L becomes

$$\frac{R_{ac}}{L} = \frac{\Delta R_{mag}}{L_{air} + \Delta L_{mag}} \quad (32)$$

then, when copper losses are comparable to magnetic losses, r_{acx} will reduce slightly with an increase in the number of turns.

From the r_{acx} plot, it can be seen that for duty cycles less than 20%, the inductor resistance increases rapidly. For duty cycles around $D = 1/48$, the resistance per unit inductance is prohibitively high and this shows the importance of extending the duty cycle to be at least 10%. This result sets a constraint in the possible power stage topologies for high conversion ratio converters. For 48–1-V IVR topologies (as surveyed in [6]) that cannot provide at least four times duty cycle extension, the inductor losses will be very high.

VII. Small-Signal Measurements With DC Bias Current

Next, the measurement of the small signal with a dc bias current is performed. Fig. 24 shows the measurement of the small-signal inductance and resistance with dc current sweep from 0 to 4.4 A, in steps of 0.4 A. With this high saturation material, the inductance does not drop. However, we can observe the increase in dc resistance at higher currents due to Joule heating.

Using these measurements, we can plot the saturation current and calculate the r_{acx} variation as a function of dc current, as shown in Fig. 25. The apparent increase in inductance is due to the error introduced by the 6.8-μH filter inductors that

Authorized licensed use limited to: Georgia Institute of Technology. Downloaded on December 09,2021 at 23:18:16 UTC from IEEE Xplore. Restrictions apply.

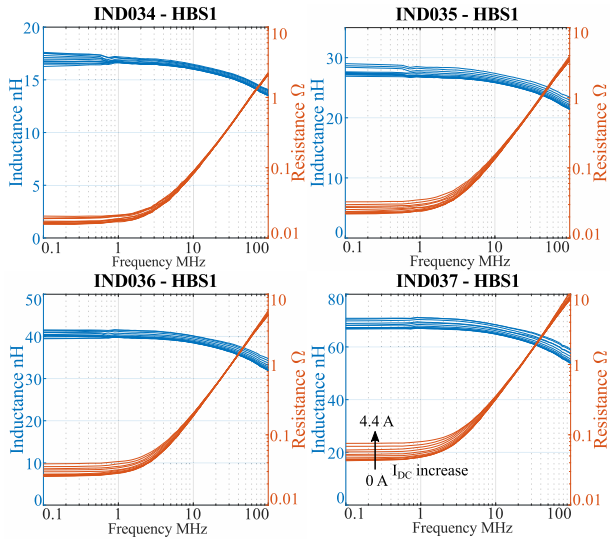

Fig. 24. Inductance and resistance spectra as a function of frequency and dc bias.

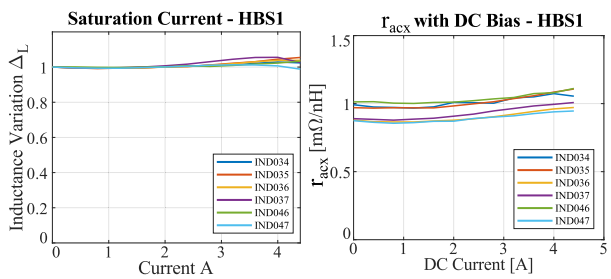

Fig. 25. Inductance and r_{acx} variation at $f_s = 5$ MHz and duty cycle $D = 0.2$.

start to saturate close at 4.5 A. The -signal r_{acx} does not change significantly with dc bias current, provided that the inductor does not saturate. The slight increment in r_{acx} is due to the increment of dc resistance due to Joule heating.

VIII. Large-Signal Measurements

The inductor IND037 and the discrete toroid were measured for the large-signal response. The inductor IND037 is only measured at 5 MHz (it becomes difficult to adjust the current ripple at lower frequencies because of its low inductance), while the discrete toroid is a measure at 3 and 5 MHz.

Using the measurement board shown in Fig. 17, the inductor voltage and current waveforms, with 0-A dc current, were recorded with different inductor current ripples and duty cycles. Fig. 26 shows some of the waveforms recorded at 5 MHz. We observe that the overshot over the inductor is accompanied with a high-slope step in the inductor current during switching transitions. This is due to the overshoot in the switching node produced by parasitic inductance (common source inductance (CSI) and gate inductance) but also because, in a GaN MOSFET, the reverse conduction mode occurs with voltages close to 2 V (as shown in its datasheet, the GaN MOSFET EPC2040 has $V_{\text{SD}} = 2.2$ V at $I_S = 0.5$ A). Therefore, during the dead-time interval t_d when both

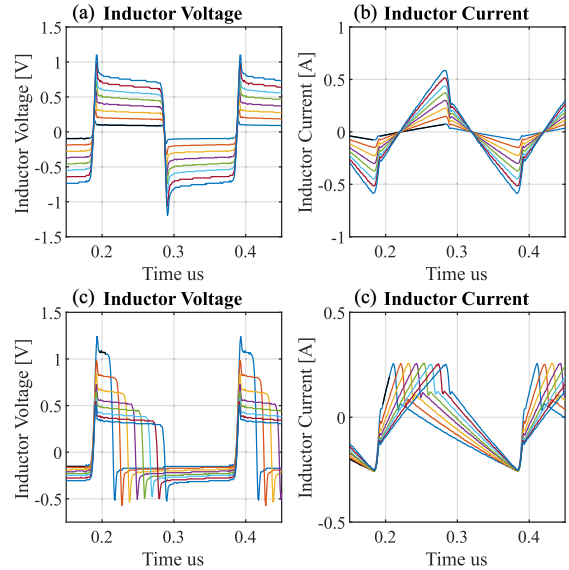

Fig. 26. Large-signal current ripple Δi_L and duty cycle D sweep. (a) and (c) Inductor voltage. (b) and (d) Inductor current.

MOSFETs are OFF, the inductor current must change such that $V_s - V + V_{\text{SD}}(i) = L(di/dt)$ or $V_{\text{SD}}(i) + V = -L(di/dt)$, depending on the transition. However, despite the distortion in the inductor current ripple, we still observed an interesting relation between the large- and small-signal losses.

The inductance L can be calculated from the average of the inductor current slope and the average inductor voltage in the interval where the inductor voltage becomes stable. The inductor current ripple Δi_L is just half the peak-to-peak current. Also, the inductor power loss P_L can be calculated as the average of the product of the inductor voltage and current waveforms. Then, with no dc current, R_{acx} can be calculated as

$$R_{\text{acx}} = \frac{P_L}{\Delta i_L^2 L}. \tag{33}$$

Tables VI and VII show the extracted parameters of IND037 from the current ripple and duty cycle sweep with a switching frequency of 5 MHz. From Table VI, we first observe an additional 7 nH of inductance added by the wiring that connect the inductor to the board. It is also observed that the R_{acx} value increases from 3.60 mΩ/nH at $\Delta i_L = 77$ mA to 4.04 mΩ/nH at $\Delta i_L = 584$ mA. Over this range, we can consider a constant value of $R_{\text{acx}} = 3.8$ mΩ/nH and conclude that the hysteresis losses are around four times larger than the small-signal losses. This gives an average factor $\kappa = 5.1$. It is interesting that, with this magnetic material, the R_{acx} metric is fairly independent of Δi_L.

From Table VII, we see that the large signal R_{acx} follows the same behavior of the small signal r_{acx} with respect to the duty cycle. With this material, the κ factor has an average value of 5.1 at 5 MHz over the entire current ripple and duty cycle sweep. This means that 20% of the ac losses are due to the small signal or linear losses and 80% are due to the magnetic hysteresis losses. This is consistent for metal polymer composited with small filler particles and no bulk

Authorized licensed use limited to: Georgia Institute of Technology. Downloaded on December 09,2021 at 23:18:16 UTC from IEEE Xplore. Restrictions apply.

TABLE VI

INDUCTOR IND037 PARAMETERS FROM LARGE-SIGNAL CURRENT RIPPLE Δi_L SWEEP AT $f_s = 5$ MHz. L_{sm} CORRESPONDS TO THE SMALL-SIGNAL INDUCTANCE

L_{sm}	nH	69.8	69.8	69.8	69.8	69.8	69.8	69.8	69.8
r_{acx}	$\frac{m\Omega}{nH}$	0.753	0.753	0.753	0.753	0.753	0.753	0.753	0.753
L	nH	77.1	76.9	75.6	75.8	75.6	76.3	76.5	76.2
Δi_L	mA	77.2	149.4	227.4	300.8	373.9	447.2	513.2	584.4
P_{AC}	mW	1.65	6.609	14.95	26.55	41.63	59.87	80.09	105.2
R_{acx}	$\frac{m\Omega}{nH}$	3.602	3.847	3.814	3.869	3.934	3.925	3.976	4.043
Ratio	$\frac{R_{acx}}{r_{acx}}$	4.786	5.112	5.068	5.141	5.227	5.215	5.283	5.372

TABLE VII

INDUCTOR IND037 PARAMETERS FROM LARGE-SIGNAL DUTY CYCLE D SWEEP AT $f_s = 5$ MHz. L_{sm} CORRESPONDS TO THE SMALL-SIGNAL INDUCTANCE

D		0.15	0.20	0.25	0.30	0.35	0.40	0.45	0.50
L_{sm}	nH	69.8	69.8	69.8	69.8	69.8	69.8	69.8	69.8
r_{acx}	$\frac{m\Omega}{nH}$	1.086	0.969	0.892	0.838	0.799	0.773	0.758	0.753
L	nH	77.9	76.1	75.6	76.1	76.5	76.0	75.9	75.5
Δi_L	mA	256.1	256.1	256.1	256.1	258.1	252.0	254.1	252.0
P_{AC}	mW	28.15	25.77	23.87	21.85	20.79	19.39	18.65	18.40
R_{acx}	$\frac{m\Omega}{nH}$	5.072	5.161	4.819	4.381	4.081	4.016	3.808	3.835
Ratio	$\frac{R_{acx}}{r_{acx}}$	5.072	5.326	5.402	5.229	5.106	5.195	5.027	5.096

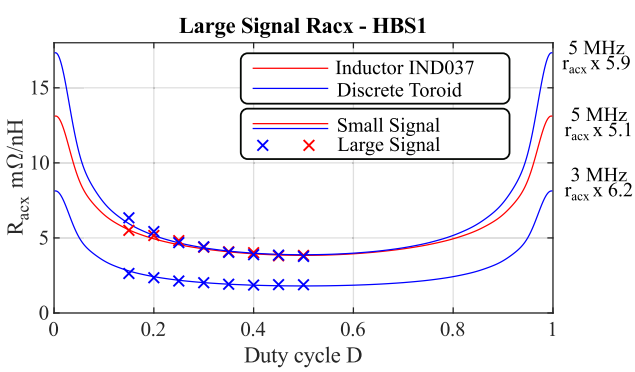

Fig. 27. Large- and small-signal comparisons at 5 and 3 MHz.

conductivity (at 5 MHz, the material loss tangent is 0.05), where it is expected to have low small-signal losses.

The discrete toroid was also analyzed and the results are compared to the embedded inductor IND037 and plotted, as shown in Fig. 27. The large signal R_{acx} is the same for both the discrete and embedded inductor in the duty cycle range of 0.2–0.8 (due to symmetry with respect $D = 0.5$). From these measurements, we observe that the large signal is proportional to the small signal by a constant, at least in a narrow frequency band, provided that the inductor is not close to saturation

$$R_{\text{acx}} = \kappa\, r_{\text{acx}}. \tag{34}$$

To determine κ, it is then necessary to measure the large signal R_{acx} at some duty cycle D and frequency f_s and then get the ratio to the small signal r_{acx} at the same duty cycle and frequency values.

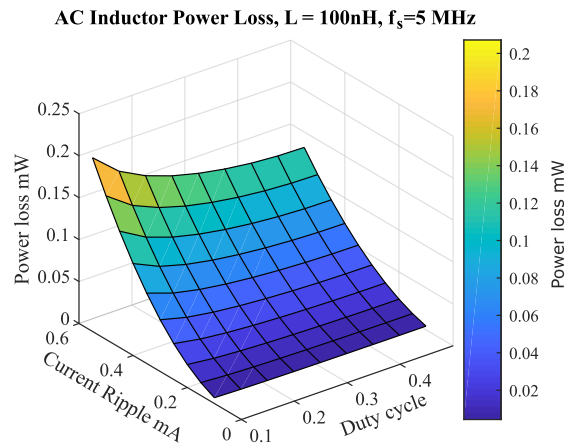

Fig. 28. AC inductor power loss surface at 5 MHz.

Based on these results and assuming that κ is constant in a narrow frequency band, it is possible to estimate the inductor power loss at some duty cycle D and switching frequency f_s with the next expression

$$P_L = I_{\text{dc}}^2\, R_{\text{dc}} + \Delta i_L^2 L\, \kappa\, r_{\text{acx}}(D, f_s) \tag{35}$$

with r_{acx} given by (7). For example, with $\kappa = 5.1$ and an embedded inductor with inductance 100 nH (regardless of its size) using HBS1, we can predict the ac power loss surface of this material, as shown in Fig. 28. With $L = 100$ nH, $\Delta i_L = 0.5$ A, duty cycle of 0.2, and $f_s = 5$ MHz, the ac power loss would be 135 mW.

However, despite the surprising linear relation of R_{acx} and r_{acx} with respect to the current ripple and duty cycle, only one material was analyzed, and therefore, it cannot be concluded that this relation will be similar for other magnetic materials or at higher frequencies. Even though the small signal r_{acx} was derived, the factor κ was found empirically, and thus, it is not clear how κ changes over a wide frequency range. More magnetic materials need to be analyzed, and improvements to the test vehicle are necessary to reduce the switching node overshoot and parasitic capacitance and inductance.

The normalization of the ac power loss with respect to the current ripple squared Δi_L^2 and inductance L seems to be an effective and a good alternative to have to determine the effective inductor volume and maximum magnetic field B_m.

IX. CONCLUSION

In this article, a new inductor metric for the inductor power loss calculation in a buck converter with a triangular current waveform, suitable up to the megahertz range, is proposed and discussed in detail. In addition, a series of high-performance embedded inductors are designed and demonstrated. These inductors have a dc resistance between 14.3 and 39.3 mΩ with a copper thickness of 25 μm and inductance between 18.8 and 70.3 nH with the Panasonic HBS1 magnetic material. Using these inductors and a high saturation current magnetic material, we have observed the surprising property that the small signal r_{acx} is related to the total or large signal R_{acx} by a constant, at least in a narrow frequency band, for a duty cycle ranging from 0.15 to 0.85 and a large range of current

Authorized licensed use limited to: Georgia Institute of Technology. Downloaded on December 09,2021 at 23:18:16 UTC from IEEE Xplore. Restrictions apply.

ripple. Up to a factor κ, the small signal r_{acx} can predict the inductor losses with good accuracy. Comparing the results of the embedded inductors with a simple discrete toroidal inductor, it is shown that the proposed power loss calculation method is highly insensitive to geometric and inductance changes. With the fabrication and measurement of a simple discrete toroidal inductor, it is possible to predict the losses of complex embedded inductors, saving a considerable amount of time and resources. The r_{acx} metric behaves as expected capturing the small-signal properties of the materials despite changing the inductor structure and amount of inductance. What needs further investigation is how R_{acx} and r_{acx} are related and how κ changes with frequency, duty cycle, and current for other materials.

We believe this simple method, where only circuit quantities, such as inductance and resistance, current ripple, and power loss, need to be measured, will allow to obtain improved designs of inductors, magnetic materials, and IVRs to power the next generation of high-performance computing (HPC) platforms. However, more materials need to be analyzed to know the limitation of this metric, for example, if it works with other ferrite or thin-film magnetics.

Acknowledgment

The authors would like to thank the fabrication support provided by the Georgia Tech Packaging Research Center (PRC) consortium members. They would also like to thank Kaladhar Radhakrishnan and Krishna Bharath, Intel Corporation, for their mentoring support and Dr. Jack Moon, School of Materials Science and Engineering, Georgia Institute of Technology, for helping in material characterization.

References

[1] S. Mappus, "Power converter topology trends," PSMA 2015 Power Technology Roadmap Presentations, Oct. 2014.

[2] C. Fei, M. H. Ahmed, F. C. Lee, and Q. Li, "Dynamic bus voltage control for light load efficiency improvement of two-stage voltage regulator," in *Proc. IEEE Energy Convers. Congr. Expo. (ECCE)*, Sep. 2016, pp. 1–8.

[3] E. A. Burton *et al.*, "FIVR—Fully integrated voltage regulators on 4th generation Intel coreT SoCs," in *Proc. IEEE Appl. Power Electron. Conf. Expo. (APEC)*, Mar. 2014, pp. 432–439.

[4] H. Torun *et al.*, "Design space exploration of power delivery in heterogeneous integration," in *Proc. GOMACTECH*, Mar. 2019.

[5] K. Radhakrishnan, M. Swaminathan, and B. K. Bhattacharyya, "Power delivery for high-performance microprocessors—Challenges, solutions, and future trends," *IEEE Trans. Compon., Packag., Manuf. Technol.*, vol. 11, no. 4, pp. 655–671, Apr. 2021.

[6] M. Gong, X. Zhang, and A. Raychowdhury, "Non-isolated 48 V-to-1 V heterogeneous integrated voltage converters for high performance computing in data centers," in *Proc. IEEE 63rd Int. Midwest Symp. Circuits Syst. (MWSCAS)*, Aug. 2020, pp. 411–414.

[7] J. M. Wright, D. W. Lee, A. Mohan, A. Papou, P. Smeys, and S. X. Wang, "Analysis of integrated solenoid inductor with closed magnetic core," *IEEE Trans. Magn.*, vol. 46, no. 6, pp. 2387–2390, Jun. 2010.

[8] P. R. Morrow, C.-M. Park, H. W. Koertzen, and J. T. DiBene, "Design and fabrication of on-chip coupled inductors integrated with magnetic material for voltage regulators," *IEEE Trans. Magn.*, vol. 47, no. 6, pp. 1678–1686, Jun. 2011.

[9] N. Sturcken *et al.*, "A 2.5D integrated voltage regulator using coupled-magnetic-core inductors on silicon interposer delivering 10.8 A/mm^2," in *IEEE Int. Solid-State Circuits Conf. (ISSCC) Dig. Tech. Papers*, Feb. 2012, pp. 400–402.

[10] N. Sturcken, R. Davies, C. Cheng, W. E. Bailey, and K. L. Shepard, "Design of coupled power inductors with crossed anisotropy magnetic core for integrated power conversion," in *Proc. 27th Annu. IEEE Appl. Power Electron. Conf. Expo. (APEC)*, Feb. 2012, pp. 417–423.

[11] S. S. Boon, D. H. S. Wee, R. Salahuddin, and R. P. Singh, "Magnetic inductor integration in FO-WLP using RDL-first approach," in *Proc. IEEE 21st Electron. Packag. Technol. Conf. (EPTC)*, Dec. 2019, pp. 18–22.

[12] M. S. Lekas, R. Davies, and N. Sturcken, "Magnetic thin-film inductors with induced radial anisotropy for improved inductance density," *IEEE Magn. Lett.*, vol. 10, pp. 1–4, 2019.

[13] Y.-C. Hsieh, S.-Y. Lin, C.-Y. Kung, P.-N. Lee, and C.-C. Wang, "Ultra low profile power inductor integrated in wafer level package," in *Proc. IEEE 21st Electron. Packag. Technol. Conf. (EPTC)*, Dec. 2019, pp. 175–178.

[14] Y. Dou, Z. Ouyang, P. Thummala, and M. A. E. Andersen, "PCB embedded inductor for high-frequency ZVS SEPIC converter," in *Proc. IEEE Appl. Power Electron. Conf. Expo. (APEC)*, Mar. 2018, pp. 98–104.

[15] R. Murphy, Z. Pavlovic, P. McCloskey, C. O Mathuna, S. O'Driscoll, and G. Weidinger, "PCB embedded toroidal inductor for 2 MHz point-of-load converter," in *Proc. 11th Int. Conf. Integr. Power Electron. Syst.*, Mar. 2020, pp. 1–5.

[16] C. O. Mathúna, N. Wang, S. Kulkarni, and S. Roy, "Review of integrated magnetics for power supply on chip (PwrSoC)," *IEEE Trans. Power Electron.*, vol. 27, no. 11, pp. 4799–4816, Nov. 2012.

[17] S. Yue, Y. Li, Q. Yang, X. Yu, and C. Zhang, "Comparative analysis of core loss calculation methods for magnetic materials under non-sinusoidal excitations," *IEEE Trans. Magn.*, vol. 54, no. 11, pp. 1–5, Nov. 2018.

[18] C. Alvarez *et al.*, "Design and demonstration of single and coupled embedded toroidal inductors for 48 V to 1 V integrated voltage regulators," in *Proc. IEEE 70th Electron. Compon. Technol. Conf. (ECTC)*, Jun. 2020, pp. 405–413.

[19] J. Li, T. Abdallah, and C. R. Sullivan, "Improved calculation of core loss with nonsinusoidal waveforms," in *Proc. 36th IEEE Ind. Appl. Conf. Rec. Annu. Meeting (IAS)*, vol. 4. Sep./Oct. 2001, pp. 2203–2210.

[20] P. S. Shenoy *et al.*, "A 5 MHz, 12 V, 10 A, monolithically integrated two-phase series capacitor buck converter," in *Proc. IEEE Appl. Power Electron. Conf. Expo. (APEC)*, Mar. 2016, pp. 66–72.

[21] A. Lidow, J. Strydom, M. de Rooij, and D. Reusch, *GaN Transistors for Efficient Power Conversion*. Hoboken, NJ, USA: Wiley, 2015.

[22] C. Alvarez, M. Bellaredj, and M. Swaminathan, "Open and closed loop inductors for high-efficiency system-on-package integrated voltage regulators," in *Proc. IEEE 69th Electron. Compon. Technol. Conf. (ECTC)*, May 2019, pp. 1672–1679.

[23] S. Barg, K. Ammous, H. Mejbri, and A. Ammous, "An improved empirical formulation for magnetic core losses estimation under nonsinusoidal induction," *IEEE Trans. Power Electron.*, vol. 32, no. 3, pp. 2146–2154, 2017, doi: 10.1109/TPEL.2016.2555359.

Claudio Alvarez Barros received the B.S. degree in electrical engineering from the Universidad de Santiago de Chile, Santiago, Chile, in 2009, and the M.S. and Ph.D. degrees from the Georgia Institute of Technology, Atlanta, GA, USA, in 2019 and 2021, respectively.

From 2010 to 2012, he worked in the international ALMA Radio Observatory. After that, he worked in other companies as an electronic and robotic engineer. After receiving his Ph.D. degree, he joined Intel Corporation, Chandler, AZ, USA, as a Senior Analog Engineer.

Dr. Alvarez Barros was granted with a Fulbright fellowship from the U.S. government and a CONICYT scholarship from the government of Chile to pursue the Ph.D. degree in USA in 2017.

Prahalad Murali received the B.Tech. degree in metallurgical and materials engineering from the National Institute of Technology at Tiruchirappalli (NITT), Tiruchirappalli, India, in 2019. He is currently pursuing the Ph.D. degree in materials science and engineering with the 3D Systems Packaging Research Center, Georgia Institute of Technology, Atlanta, GA, USA, advised by Prof. Madhavan Swaminathan and Prof. Mark Losego.

His current research interests include fabrication of package-embedded inductors and synthesis of magnetic materials for dc–dc converters.

Authorized licensed use limited to: Georgia Institute of Technology. Downloaded on December 09,2021 at 23:18:16 UTC from IEEE Xplore. Restrictions apply.

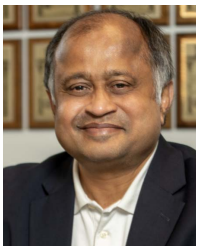

Madhavan Swaminathan (Fellow, IEEE) received the M.S. and Ph.D. degrees in electrical engineering from Syracuse University, Syracuse, NY, USA, in 1989 and 1991, respectively.

He is currently the John Pippin Chair in Microsystems Packaging and Electromagnetics with the School of Electrical and Computer Engineering (ECE), Professor in electronics and communication engineering with a joint appointment at the School of Materials Science and Engineering (MSE), and the Director of the 3D Systems Packaging Research Center (PRC), Georgia Tech (GT), Atlanta, GA, USA. He also serves as the Site Director for the NSF Center for Advanced Electronics through Machine Learning (CAEML) and the Theme Leader for Heterogeneous Integration at the SRC JUMP ASCENT Center. Prior to joining GT, he was with IBM working on packaging for supercomputers. He is the author of more than 530 refereed technical publications and holds 31 patents. He is the primary author and a coeditor of three books and five book chapters and the founder and co-founder of two startup companies.

Dr. Swaminathan is the Founder of the IEEE Conference on Electrical Design of Advanced Packaging and Systems (EDAPS), a premier conference sponsored by the IEEE Electronics Packaging Society (EPS). He has served as a Distinguished Lecturer for the IEEE Electromagnetic Compatibility (EMC) Society.

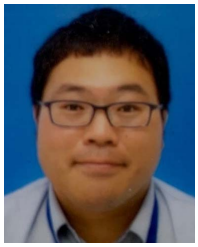

Oishi Yusuke received the master's degree in biomolecular engineering from Kyoto Institute of Technology, Kyoto, Japan, in 2010.

He has been with Panasonic Corporation, Kadoma, Japan, since 2010, where he is currently a Staff Engineer with the Panasonic Electronic Materials Division. Over his career, he has conducted formulation design of epoxy molding compound for semiconductor packages, including inductor.

Takashiro Junichi received the master's degree in chemical engineering from Tokyo Institute of Technology, Tokyo, Japan, in 2013.

He has been with Panasonic Corporation since 2013, where he is currently an Engineer with the Panasonic Electronic Materials Division. Over his career, he has conducted formulation design of sheet form epoxy molding compound for semiconductor packages, including inductor.

Nagatsuka Ryo received the master's degree in chemical bioengineering from Kansai University, Suita, Japan, in 2017.

He has been with Panasonic Corporation, Kadoma, Japan, since 2017, where he is currently an Engineer with the Panasonic Electronic Materials Division. Over his career, he has conducted formulation design of epoxy molding compound for semiconductor packages, including inductor.

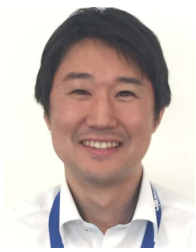

Naoki Watanabe received the master's degree in chemical engineering from Kyoto University, Kyoto, Japan, in 2005.

He has been with Panasonic Corporation, Kadoma, Japan, since 2005, where he is currently a Senior Research Manager with the Panasonic Electronic Materials Division. Over his career, he has primarily conducted research on semiconductor packaging materials, such as epoxy molding compounds and capillary underfills. Most recently, he has been working in USA developing advanced magnetic materials for embedded inductors. He currently works in Mountain View, CA, USA, and will return to Japan in 2022.

Authorized licensed use limited to: Georgia Institute of Technology. Downloaded on December 09,2021 at 23:18:16 UTC from IEEE Xplore. Restrictions apply.